Anisotropic enhancement of piezoelectricity in the optical properties of laterally coupled InAs/GaAs self-assembled quantum dots

Pilkyung Moon and Euijoon Yoon

Department of Materials Science and Engineering, Compound Semiconductor Epitaxy Laboratory,
Seoul National University, Seoul 151-742, Korea

Weidong Sheng

Department of Physics, Fudan University, Shanghai 200433, People's Republic of China

Jean-Pierre Leburton

Department of Electrical and Computer Engineering and Department of Physics, Beckman Institute for Advanced Science and
Technology, University of Illinois at Urbana-Champaign, Urbana, Illinois 61801, USA

We investigated the electronic and optical properties of self-assembled laterally double InAs/GaAs quantum dots coupled along the [110] and [1$\bar{1}$0] directions with varying interdot distances. The coupling region provides a stronger confinement for both electrons and holes than in the center of each dot due to the weak compressive strain and positive biaxial strain in the region. The lateral coupling along the [110] ([1$\bar{1}$0]) direction enhances the negative (positive) piezoelectric potential in the coupling region and lowers (raises) the potential in the middle of each dot. As a result, the piezoelectric potential decreases the splitting between the two transitions from the bonding s orbitals to the two coupled p orbitals in quantum dots coupled along the [1$\bar{1}$0] direction and increases the splitting in the quantum dots coupled along the [110] direction. The direction of coupling is clearly distinguishable by the polarization of intraband transition since most transitions are polarized along the axis passing through the two dots. Lateral coupling enhances the polarization anisotropy of interband absorption spectra. In the presence of the piezoelectric potential, quantum dots coupled along the [110] direction exhibit larger redshift of the lowest exciton energies when the distance between the two dots is sufficiently close and have smaller exciton binding energies than quantum dots coupled along the [1$\bar{1}$0] direction.

I. INTRODUCTION

Coupled quantum dots (QDs) have attracted much interest since coupling between the dots considerably changes the electronic structures and the optical properties of the dots.[1–9] Until recently, coupled QDs have been fabricated by cleaved edge overgrowth,[1] vertical stacking of the self-assembled QDs (VCQDs),[2] and tunable gates.[3] Recent advances in the quantum dot growth techniques enable the fabrications of the laterally coupled self-assembled quantum dots (LCQDs),[4,10,11] and optical measurements provide a systematic way to study the electronic coupling.[4,5] Unlike VCQDs which have one-dimensional freedom along the growth direction, the LCQDs enable the coupling in two dimensions, in principle. However, although many theoretical works[6–9] have investigated the excitonic spectra, the effects of external fields on the electronic structures, and the effects of substrate orientations on the optical properties of LCQDs, little attention has been paid to the optical anisotropy induced by different coupling directions, i.e., [110] and [1$\bar{1}$0].

It is well known that the two lower energy p states of InAs/GaAs single QD (SQD) [Fig. 1(a)] are oriented along the [110] ($p_{[110]}$) and [1$\bar{1}$0] ($p_{[1\bar{1}0]}$) directions due to the atomistic and piezoelectric C_{2v} symmetries of zinc-blende structures.[12–14] When two QDs are vertically coupled [Fig. 1(b)], both the two p states of the dots form π molecu-

lar orbitals,[15] analogous to the two p states oriented perpendicular to the axis passing through the two atoms of diatomic molecules. Since the spatial overlap between the $p_{[110]}$ states on both dots is similar to that between the $p_{[1\bar{1}0]}$ states, the bonding-antibonding splitting of the $\pi(p_{[110]})$ orbitals exhibits almost the same magnitude as those of the $\pi(p_{[1\bar{1}0]})$ orbitals. On the contrary, in LCQDs, the molecular orbitals (coupled states) of the $p_{[110]}$ and the $p_{[1\bar{1}0]}$ states are clearly distinguishable by their splitting energies when two dots are coupled along the lateral directions of [110] or [1$\bar{1}$0]. The SQD $p_{[110]}$ ($p_{[1\bar{1}0]}$) states form σ (π) molecular orbitals in the QDs coupled along the [110] direction ("[110] LCQDs" in
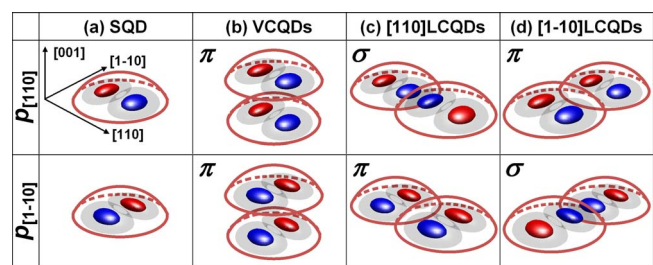
FIG. 1. (Color online) (a) The electron probability densities of the first ($p_{[110]}$) and the second ($p_{[1\bar{1}0]}$) excited states of SQD, and their coupled structures [(b) VCQDs, (c) [110] LCQDs, and (d) [1$\bar{1}$0] LCQDs]. σ and π denote the types of the molecular orbitals.

Fig. 1(c)), whereas the SQD $p_{[1\bar{1}0]}$ ($p_{[110]}$) states form σ (π) molecular orbitals in the QDs coupled along the $[1\bar{1}0]$ direction ("$[1\bar{1}0]$ LCQDs" in Fig. 1(d)).[16] Since the *p* states parallel to the axis passing through the two dots have larger spatial overlap than those perpendicular to the axis, the σ molecular orbitals exhibit larger bonding-antibonding splitting than the π orbitals, as in the case of the diatomic molecular orbitals. In addition, since both dots in LCQDs have symmetric strain profiles and piezoelectric potential distributions, unlike the asymmetric ones of VCQDs,[15,17,18] there is no hole (electron) localization in none of the individual dot.

In this paper, we investigate the electronic and optical properties of self-assembled LCQDs by varying the direction of coupling and the interdot distance. This paper is organized as follows. In Sec. II we present the structure models and theoretical models used in this work. The strain and the piezoelectric potential profiles, the confined energy levels of both electrons and holes, and the optical properties of LCQDs are shown in Sec. III. Finally, the concluding Sec. IV summarizes the results.

II. STRUCTURE MODELS AND THEORETICAL METHODS

A. Structure model

To investigate the effects of coupling directions on the electronic structures of LCQDs, we compare two LCQDs with different coupling directions: (i) QDs coupled along the [110] direction (Fig. 1(c): [110] LCQDs) and (ii) $[1\bar{1}0]$ direction (Fig. 1(d): $[1\bar{1}0]$ LCQDs). Each QD is a lens-shaped InAs dot with a base length of 24.3 nm and a height of 3.96 nm grown on GaAs (001) substrate. In addition, we also investigate the effects of coupling distances by varying the interdot distance (i.e., the distance between the dot edges at the base plane): (i) infinitely separated dots (equivalent to "SQD"), (ii) 3.44 nm separated dots [LCQDs (+3.44 nm)], (iii) 0.24 nm separated dots [LCQDs (+0.24 nm)], (iv) 2.96 nm overlapped dots [LCQDs (−2.96 nm)], and (v) 6.15 nm overlapped dots [LCQDs (−6.15 nm)].

B. Equilibrium atomic positions and piezoelectric potential

We used a valence force field (VFF) method with Keating's potential[19] and Martin's parameters[20] to obtain the strain profiles of the structures. The VFF method provides more accurate strain profiles than the continuum elasticity method as it considers the actual atomistic symmetry (C_{2v} for zinc-blende structure) and anharmonic effects which are important in systems with large lattice mismatches and with rapidly varying strain profiles (e.g., at the interface between InAs and GaAs). Due to the long-range behavior of the atomistic distortion, we used a sufficiently large supercell to relax the atomic positions of each structure: $137 \times 137 \times 120$ unit cells for SQD system where the dot occupies $43 \times 43 \times 7$ unit cells, and $169 \times 169 \times 120$ unit cells for LCQDs where the coupled dots occupy approximately $77 \times 77 \times 7$ unit cells (depending on the interdot distance). We imposed a fixed boundary condition on the base plane of the

supercell, a free-standing boundary condition on the top, and periodic boundary conditions on the four sides. The size of the supercell is large enough to minimize the undesirable interactions with periodic images in lateral directions. We calculate the equilibrium atomic positions by minimizing the strain energy with a conjugate gradient method[21] and obtain the local strain tensor at each atomic site from the coordinates of its four nearest-neighboring atoms.[22]

Due to the lack of fourfold symmetry in zinc-blende materials, two different coordinate systems can be used which are identified by the atomistic [111] directions: (i) from the metallic atom to the nonmetallic atom[23] or (ii) from the nonmetallic atom to the metallic atom.[24] The definition of the coordinate is important because the sign of the piezoelectric constant depends on the crystallographic direction. In the former definition of the coordinates, the piezoelectric constants of both InAs and GaAs are negative, while the opposite is true for the latter. In this paper, we use the former definition since this is the convention used by experimentalists.[23,25]

We calculate the piezoelectric potential V_{piezo} by solving the Poisson's equation,

$$\nabla^2 V_{\text{piezo}}(r) = -\frac{1}{\varepsilon(r)}\rho_P(r), \tag{1}$$

using a four-level multigrid method.[21] Here, $\varepsilon(r)$ corresponds to the dielectric constant of the material at position r, $\rho_P(r)$ corresponds to the piezoelectric charge density,

$$\rho_P(r) = \text{div}\left(\sum_{j,k} e_{ijk}(r)\varepsilon_{jk}(r)\right), \quad (i,j,k=x,y,z), \tag{2}$$

$e_{ijk}(r)$ corresponds to the piezoelectric constant, and $\varepsilon_{jk}(r)$ corresponds to the shear strain.

Recently, the importance of the second-order (to the shear strain tensors) terms in the piezoelectricity has been pointed out by several groups.[14,26–28] However, since the first- and second-order terms in our flat lens-shaped QD have opposite signs and have similar magnitude, they cancel each other as reported by Bester *et al.*[26] and Schliwa *et al.*[28] To simplify the problem, we calculate the piezoelectric potential up to the first-order term with classical parameters and compare the electronic structures in the absence and presence of the piezoelectric potential. Section III B exhibits the energy levels and probability densities in the absence of the piezoelectric potential (or in the presence of the first- and second-order piezoelectric potentials), and Sec. III D shows those in the presence of the (classical) first-order term.

C. Electronic structures

We calculate the wave functions and the energy levels of SQD and LCQDs by solving an eight-band $\mathbf{k}\cdot\mathbf{p}$ Hamiltonian,[29–31]

$$H = H_{\mathbf{k}\cdot\mathbf{p}} + H_{\text{strain}} + H_{\text{spin-orbit}} - eV_{\text{piezo}}, \tag{3}$$

based on Burt[32] and Foreman's method.[33,34] The effects of strain and the spin-orbit coupling are included in the $\mathbf{k}\cdot\mathbf{p}$ Hamiltonian by following Bahder's model.[30] To eliminate

TABLE I. Material parameters used in this work.

Parameter	InAs	GaAs
Lattice constant (a_{lc}) [a]	0.60583 nm	0.56532 nm
VFF parameter (α) [b]	35.18 N/m	41.19 N/m
VFF parameter (β) [b]	5.50 N/m	8.95 N/m
Fundamental gap (E_{gap}) [c]	0.42 eV	1.52 eV
VB offset (E_v) [a]	0.21 eV	0.00 eV
Spin-orbit coupling energy (Δ_{so}) [c]	0.38 eV	0.34 eV
Optical matrix parameter (E_p) [c]	22.2 eV	25.7 eV
Electron effective mass (m_e) [c]	$0.023m_0$	$0.067m_0$
Luttinger parameter (γ_1) [c]	19.67	7.65
Luttinger parameter (γ_2) [c]	8.37	2.41
Luttinger parameter (γ_3) [c]	9.29	3.28
CB hydrostatic deformation potential (a_c) [a]	−5.08 eV	−7.17 eV
VB hydrostatic deformation potential (a_v) [a]	−1.00 eV	−1.16 eV
VB shear deformation potential [100] (b) [a]	−1.8 eV	−2.0 eV
VB shear deformation potential [111] (d) [a]	−3.6 eV	−4.8 eV
Piezoelectric modulus (e_{14}) [d]	−0.045 C/m^2	−0.160 C/m^2

[a]Reference 39.
[b]Reference 20.
[c]Reference 37.
[d]Reference 23.

the spurious checkerboard solutions (i.e., the decoupling between the solutions on the subgrids with even and odd indices) arising from central difference scheme, we discretize the envelope functions on a staggered grid following Hai-Bin *et al.*[35] rather than on a collocated grid: (i) the envelope functions of electrons (F_s) are defined on a cubic grid with a spacing Δa (taken to be the lattice constant of GaAs in this work) and (ii) those of holes (F_x, F_y, F_z) are discretized on the grids which are displaced by $\Delta a/2$ along the X, Y, and Z directions, respectively. All the parameters used in this paper are listed in Table I. To avoid the spurious solutions arising from eight-band **k**·**p** method with finite difference method,[36] we use the parameters for electronic structures (spin-orbit coupling energies, optical matrix parameters, electron effective masses, and Luttinger parameters) reported by Lawaetz.[37]

III. RESULTS AND DISCUSSIONS

As seen from Fig. 1, the differences between the electronic structures of [110] and [1$\bar{1}$0] LCQDs mainly originate from the anisotropic distributions of the SQD wave functions along the [110] and [1$\bar{1}$0] directions. In a SQD with a shape symmetry higher than twofold rotations [e.g., a pyramid (C_{4v}) and a lens, a disk, or a truncated cone ($C_{\infty v}$)], the spatial anisotropy of wave functions is determined by the sum of atomistic interface effects, atomic relaxation effects, and a piezoelectric effect[23] (denoted as "level 2," "level 3," and "level 4" in Bester *et al.*,[23] respectively). To distinguish the effects of the strains and the piezoelectric potential on the electronic structures of LCQDs, we investigate the strain

profiles and the electronic structures of LCQDs in the absence of the piezoelectric potential (or in the presence of the first and the second-order piezoelectric potentials) in Secs. III A and III B and the piezoelectric potential distributions and the electronic structures in the presence of the (classical) first-order piezoelectric potential in Secs. III C and III D. In this study, the atomistic interface effect is included in the strain effects.

A. Strain profiles and band-edge potentials

We plot the (1$\bar{1}$0) cross sections of the hydrostatic ($H = \varepsilon_{xx} + \varepsilon_{yy} + \varepsilon_{zz}$) and biaxial strains [$B = \varepsilon_{zz} - 0.5 \times (\varepsilon_{xx} + \varepsilon_{yy})$] of SQD, [110] LCQDs (+0.24 nm), and [110] LCQDs (−6.15 nm) in Fig. 2, and the [110] line profiles of the strains 0.565 nm above the base planes in Figs. 3(a) and 3(c). Both the hydrostatic and biaxial strains slowly approach to zero along the growth direction of the dot[38] and rapidly decay to zero along the in-plane direction outside the dot. The hydrostatic strain is negative inside the dot and abruptly changes its sign at the interfaces between InAs and GaAs. Figures 2 and 3 show that the GaAs between the two dots of LCQDs (+0.24 nm) is more tensile strained than those on the other sides of the dots, and the InAs near the coupling region of LCQDs (−6.15 nm) is less compressed than those in the middle of the dots. The strain far from the coupling region is less affected by the coupling. The biaxial strain is positive inside the dot since a lens-shaped InAs dot embedded in GaAs matrix is laterally compressed (ε_{xx} and $\varepsilon_{yy} < 0$) and vertically dilated ($\varepsilon_{zz} > 0$). The biaxial strain reaches its maximum at the corners, especially near the coupling region, of the dots [Figs. 2(d)–2(f) and 3(c)].
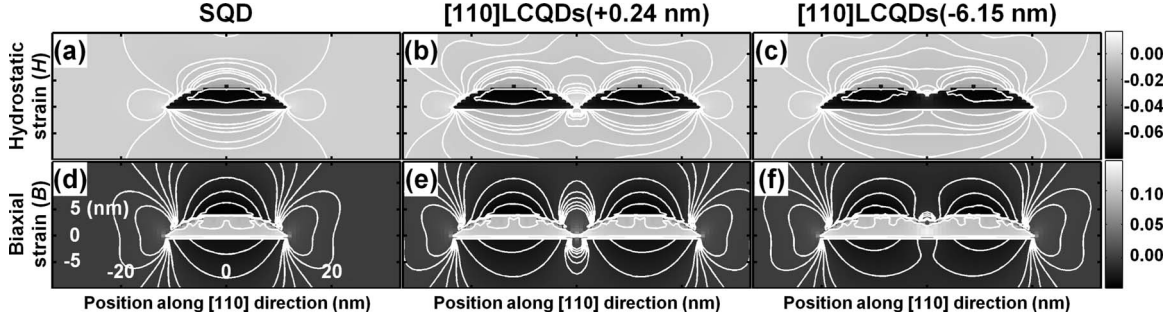
FIG. 2. $(1\bar{1}0)$ cross-sections of the hydrostatic strains of (a) SQD, (b) [110] LCQDs (+0.24 nm), and (c) [110] LCQDs (−6.15 nm), and the cross-sections of the biaxial strains of (d) SQD, (e) [110] LCQDs (+0.24 nm), and (f) [110] LCQDs (−6.15 nm).

Table II shows the minimum, maximum, and average hydrostatic strains inside the dots. The maximum strains exhibit large fluctuations since the strains located at the interfaces between InAs and GaAs strongly depend on the atomic configurations at the interfaces. On the contrary, the minimum and the average strains are monotonically weakened as the interdot distance shrinks: the average strain of LCQDs (+3.44 nm) is 0.0002 stronger (more compressed) than that of SQD, whereas that of LCQDs (−6.15 nm) is 0.0006 weaker (less compressed) than that of SQD. Since the electron and hole wave functions are not uniformly distributed inside the dots, the more accurate effects of the strains on the electron and hole energies are estimated by the summation of the strain weighted by the electron probability distributions in Sec. III B. The weighted sums for the electron ground states (the last row of Table II) are 0.006–0.007 (i.e., 10%) larger than the arithmetic means throughout the whole structures since electrons prefer the sites with weaker compressive strain. In LCQDs (−6.15 nm), the electron ground state feels 0.0018–0.0019 higher hydrostatic strain than that of SQD. Since the conduction-band (CB) deformation potential (a_c) of InAs is −5.08 eV,[39] the compressive strain raises the electron ground states of LCQDs (+3.44 nm) by about 1.52 meV than that of SQD and lowers those of LCQDs (−6.15 nm) by 9.14–9.65 meV.

Figure 4 shows the strain-modified band-edge potentials near the fundamental gap of InAs by using the **k·p** method: electron (CB), heavy-hole (HH), light-hole (LH), and spin-orbit split-off (SO) bands. Each band is twofold degenerated by spin. A compressive (tensile) strain (H) increases (reduces) the gap by

$$\Delta E_{\text{gap}}(H) = \Delta E_{\text{CB}}(H) + \Delta E_{\text{VB}}(H) = (a_c + a_v)H, \quad (4)$$

whereas a biaxial strain (B) lifts the degeneracy of HH and LH by[40]

$$\Delta E_{\text{HH-LH}}(B) = -\tfrac{1}{2}(3bB - \Delta + \sqrt{\Delta^2 + 2\Delta bB + 9b^2B^2}). \quad (5)$$

Here, a_c and a_v correspond to the CB and valence-band (VB) deformation potentials, b corresponds to the shear deformation potential, and Δ corresponds to the spin-orbit splitting energy. In this work, we followed the sign convention of a_v by Vurgaftman *et al.*[39] although the sign remains somewhat controversial (e.g., Wei and Zunger[41] reported a_v with an opposite sign). Figure 2(d) shows that the biaxial strain changes sign in the growth direction: negative below the dot, positive inside the dot, and negative above the dot. In contrast, the biaxial strain is always positive in the lateral direction. As a consequence, in VCQDs, the GaAs between the dots acts as a strong barrier for the dominant component (HH) of hole states, and this causes the HH to be more localized inside the dots.[18] In contrast, the HH in LCQDs stays attractive even between the dots, resulting in less confinement. In LCQDs (−6.15 nm) [Fig. 4(c)], the coupling region provides strong confinements for both HH (by the strong positive biaxial strain) and CB (by the weak compressive strain).

Since the strain obtained by VFF follows the C_{2v} atomic symmetry of zinc-blende material, there is a weak but finite anisotropy between the [110] and $[1\bar{1}0]$ profiles of the strain.[22] We plot the difference between the hydrostatic (biaxial) strains along the [110] direction of [110] LCQDs and

TABLE II. The minimum, maximum, and average hydrostatic strains of SQD and LCQDs as a function of interdot distance (d). The last row shows the sum of the strain weighted by the electron ground-state probability density.

d (nm)	$[1\bar{1}0]$ LCQDs				SQD	[110] LCQDs			
	+3.44	+0.24	−2.96	−6.15	∞	−6.15	−2.96	+0.24	+3.44
Min	−0.0835	−0.0835	−0.0834	−0.0832	−0.0832	−0.0833	−0.0835	−0.0835	−0.0835
Max	−0.0510	−0.0478	−0.0402	−0.0492	−0.0510	−0.0496	−0.0362	−0.0438	−0.0502
Average	−0.0756	−0.0754	−0.0750	−0.0748	−0.0754	−0.0748	−0.0750	−0.0754	−0.0756
Weighted sum	−0.0692	−0.0690	−0.0683	−0.0671	−0.0689	−0.0670	−0.0682	−0.0690	−0.0692
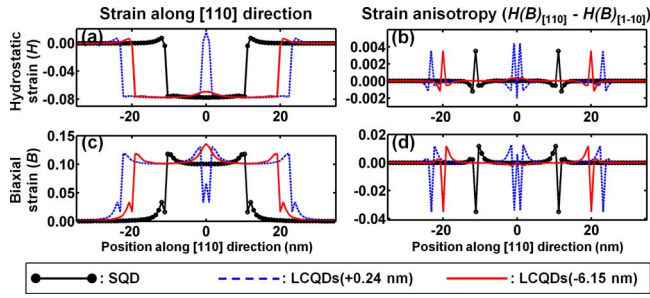
FIG. 3. (Color online) [110] line profiles of the strains 0.565 nm above the base planes of SQD, LCQDs (+0.24 nm), and LCQDs (−6.15 nm). (a) Hydrostatic strains, (b) the difference between the hydrostatic strains along the [110] and [1$\bar{1}$0] directions, (c) biaxial strains, and (d) the difference between the biaxial strains along the [110] and [1$\bar{1}$0] directions.

the [1$\bar{1}$0] direction of [1$\bar{1}$0] LCQDs in Fig. 3(b) and 3(d). The strain anisotropy reaches its extremum at the interfaces between InAs and GaAs and decays to zero as the distance from the interfaces increases. The anisotropy between the [110] and [1$\bar{1}$0] directions of the CB potentials is $\Delta E_{CB}(\Delta H)$, whereas that of the VB potentials is the sum of $\Delta E_{VB}(\Delta H)$ and $0.5 \times \Delta E_{HH-LH}(\Delta B)$. Since the absolute value of b(InAs) is larger than a_v(InAs) (Table I) and the magnitude of ΔB [Fig. 3(d)] is much larger than that of ΔH [Fig. 3(b)], the anisotropy of the VB potentials is mainly determined by the anisotropy of the biaxial strain.

B. Electronic structures in the absence of the piezoelectric potential

1. Conduction band

We plot the electron energies and wave functions of SQD and LCQDs as a function of interdot distance (d) in Fig. 5. The black, red, and blue lines in Figs. 5(a) and 5(b) [Fig. 5(c)] represent the electron energies of the bonding (solid lines) and antibonding (dashed lines) molecular orbitals originate from the SQD ground, the first, and the second

excited states (the third, the fourth, and the fifth excited states), respectively. Each state is doubly degenerated by spin. The left-half side of Figs. 5(a)–5(c) exhibit the energies of [1$\bar{1}$0] LCQDs and the right-half side show those of [110] LCQDs. We plot the electron probability densities of the lower states [Figs. 5(a) and 5(b)] in Fig. 5(d) and those of the higher states [Fig. 5(c)] in Fig. 5(e). The isosurfaces with light and dark colors enclose 85 and 30% of the state densities, and the inner isosurfaces (dark color surfaces) are colored by their relative phases.

Since the anisotropy arising from the strain is weak inside the dot, each SQD state is well described by the axial angular momentum along the growth direction,[42]

$$L_n = \int dz \int \rho d\rho \left| \int F_n(\rho, \phi, z) \frac{e^{im\phi}}{\sqrt{2\pi}} d\phi \right|^2,$$

$$(F_n : \text{envelope of } n\text{th band}). \quad (6)$$

We label the lower molecular orbitals in Figs. 5(a), 5(b), and 5(d) by L_n (1s, 1p_1, 1p_2, 1d_1, 1d_2, and 2s), the angular momentum along the axis passing through the two dots (σ for the angular momentum of 0 and π for 1), and the symmetry under inversion (g for even and u for odd). The antibonding orbitals are labeled with an asterisk (*). For simplicity, the angular momentum along the axis and the symmetry under inversion are omitted in Figs. 5(c) and 5(e).

Sometimes it is more convenient to express each state by the quantum numbers $|n_1, n_2, n_3\rangle$ of three-dimensional harmonic oscillator where n_1, n_2, and n_3 correspond to the number of nodes along the [110], [1$\bar{1}$0], and [001] directions (or equivalently, the "pseudoquantum number ($|n_1 n_2 n_3\rangle$)" introduced by Stier et al.[13]). In the SQD with $C_{\infty v}$ symmetry, the 1p_1 ($|1,0,0\rangle$) and 1p_2 ($|0,1,0\rangle$) states and the 1d_1 ($|2,0,0\rangle - |0,2,0\rangle$) and 1$d_2$ ($|1,1,0\rangle$) states are degenerated by symmetry. However, since the C_{2v} symmetry of the zinc-blende strains applies a weak but finite anisotropy between the [110] and [1$\bar{1}$0] directions of the wave functions, the degeneracy between the 1p_1 and 1p_2 states is lifted by 0.212 meV and
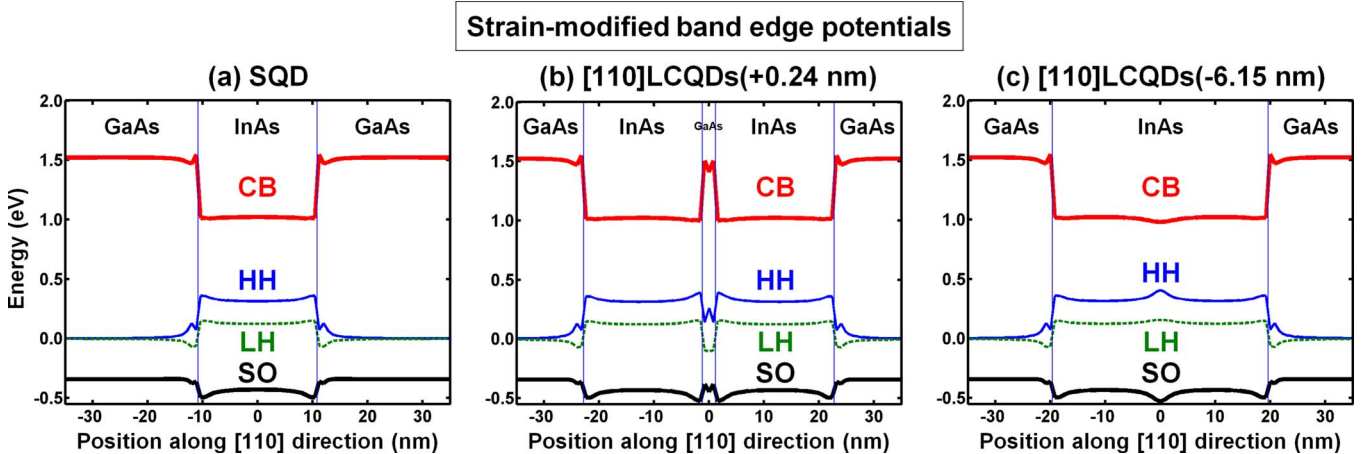
FIG. 4. (Color online) Eight strain-modified band-edge potentials near the fundamental gap of InAs calculated from an eight-band **k·p** method (each band is twofold degenerated by spin).
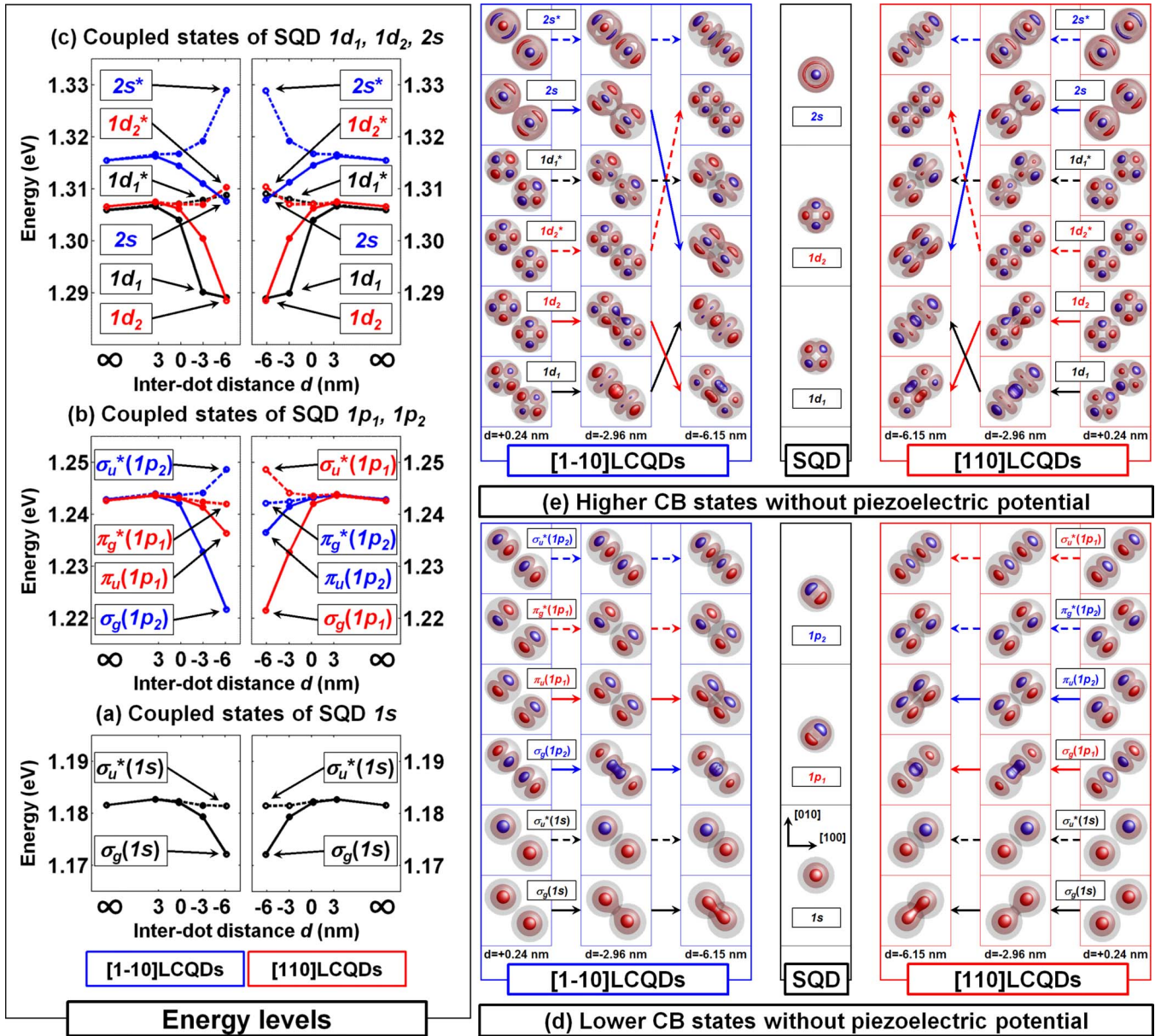
FIG. 5. (Color online) The energy levels of the coupled states originate from the SQD (a) $1s$, (b) $1p_1$ and $1p_2$, and (c) $1d_1$, $1d_2$, and $2s$ states in the absence of the piezoelectric potential (or in the presence of the first and the second-order piezoelectric potentials, see text). And the electron probability densities of the coupled states originate from the SQD (d) $1s$, $1p_1$, and $1p_2$, and (e) $1d_1$, $1d_2$, and $2s$ states.

that between the $1d_1$ and $1d_2$ states is lifted by 0.664 meV. We note the following features:

(i) *SQD states and the anisotropy*. In the absence of the piezoelectric potential, the first and second excited states of SQD are oriented along the [110] and [1$\bar{1}$0] directions, respectively. However, as seen from their small energy differences, the anisotropy between the [110] and [1$\bar{1}$0] directions induced by the strain is very weak. As a consequence, most of the states do not exhibit clear preferential directions in their probability distributions: the $1s$ and $2s$ states of SQD are circularly symmetric, and the $1d_1$ and $1d_2$ states have almost symmetric spatial distributions along the [110] and [1$\bar{1}$0] directions.

(ii) *LCQDs states*. The ground-state energy of LCQDs

(+3.44 nm) is 1.14 meV higher than that of SQD and that of LCQDs (−6.15 nm) is 9.43 meV lower than that of SQD, as expected from the compressive strain weighted by the ground-state probability density [1.52 meV for LCQDs (+3.44 nm) and −9.14−−9.65 meV for LCQDs (−6.15 nm) in Sec. III A]. Since the spatial overlap between the dot wave functions of LCQDs (+3.44 nm) is very small, the coupled states exhibit a very small energy splitting between the bonding and antibonding orbitals. As the interdot distance becomes sufficiently short, the energy splitting between the bonding and antibonding orbitals increases. The bonding orbital has a high electron probability density in the coupling region, whereas the antibonding orbital has a node in that region. In addition, the phase of the states changes sign on both sides of the node as shown by the two color

surfaces in the figures. Since the lateral coupling imposes a strong anisotropy between the directions parallel and perpendicular to the coupling direction, the degeneracy between the $1p_1$ and $1p_2$ orbitals (and that between the $1d_1$ and $1d_2$ orbitals) is lifted. As seen from Figs. 1, 5(b), and 5(d), the SQD $1p_1$ state $(p_{[110]})$ forms π orbitals $[\pi_u(1p_1)$ and $\pi_g^*(1p_1)]$ with a small bonding-antibonding splitting (6.13 meV) in $[1\bar{1}0]$ LCQDs (-6.15 nm), whereas the $1p_2$ state $(p_{[1\bar{1}0]})$ forms σ molecular orbitals $[\sigma_g(1p_2)$ and $\sigma_u^*(1p_2)]$ with a larger splitting (28.3 meV). On the contrary, the $1p_1$ state forms σ orbitals $[\sigma_g(1p_1)$ and $\sigma_u^*(1p_1)]$ in $[110]$ LCQDs (-6.15 nm) with a larger splitting, whereas the $1p_2$ state forms π orbitals $[\pi_u(1p_2)$ and $\pi_g^*(1p_2)]$ with a smaller one. Since most of the electron probabilities are found inside each dot, where the anisotropy imposed by the strains is weak, there is no clear difference between the probability distributions and energies of σ orbitals in $[1\bar{1}0]$ and $[110]$ LCQDs, except their orientations. The same is true for the π orbitals.

Many authors[15,17,18] reported the localized states (either in top or in bottom QD) in VCQDs due to the asymmetric strain profiles and dot geometries. However, since both dots in LCQDs have symmetric strain profiles and dot geometries, there is no such a localized state in either QD.

(iii) *Higher excited states*. Since the higher excited states of SQD ($1d_1$, $1d_2$, and $2s$) have no preference between the $[110]$ and $[1\bar{1}0]$ directions, their coupled states form the same types of the molecular orbitals in both $[110]$ and $[1\bar{1}0]$ LCQDs with the same bonding-antibonding splitting. Unlike the probability distributions of the lower excited states, those of the higher excited states exhibit larger deformation from the SQD ones, especially when the distance between the two dots is sufficiently close: e.g., the coupled $1d_1$ (and $2s$) states [Fig. 5(e)]. Thus, we distinguished each higher excited state by its orbital character, not by its pseudoquantum number. At first, we distinguished the bonding and antibonding orbitals from the node and the phase information of the envelope functions (antibonding orbital changes its phase at the node by 180°) and put them in order by their relative energies (the energy of antibonding orbital is higher than that of the matching bonding orbital). Then, we labeled the bonding and antibonding orbitals of the SQD $1d_2$ state since these states are less deformed by the coupling along the $[110]$ and $[1\bar{1}0]$ directions due to their high probability densities along the $[100]$ and $[010]$ directions. Finally, the remaining states (the coupled $1d_1$ and $2s$ states) are distinguished by their orbital characters. Since the SQD $2s$ state exhibits a dominant s orbital character (99.8%), whereas the $1d_1$ state has an almost d orbital character (93.3%), the coupled $2s$ states also have sizable s orbital characters. We calculated the orbital characters of LCQDs by evaluating Eq. (6) in either dot. Although such evaluation generate some errors which originate from the truncation of the wave functions outside the dot (e.g., the s orbital character of the SQD $2s$ state is decreased to 87.7% by the truncation), still the coupled $2s$ states are clearly distinguishable by their large s orbital characters [e.g., the $1d_2$, $1d_1$, $2s$, $1d_1^*$, $1d_2^*$, and $2s^*$ orbitals of $[1\bar{1}0]$ LCQDs (-6.15 nm) in Fig. 5(e) has 0.01, 1.40, 31.2, 7.05, 0.01, and 24.9% s characters].

The lateral coupling induces a strong anisotropy between the $[110]$ and $[1\bar{1}0]$ directions of the probability distributions. For example, the SQD $1d_1$ state, which is isotropic along the $[110]$ and $[1\bar{1}0]$ directions, exhibits a clear preferential direction by lateral coupling: each individual dot wave function of the $1d_1$ bonding orbital is oriented along the axis passing through the two dots, whereas that of the $1d_1^*$ antibonding orbital is oriented perpendicular to the axis. The coupled $2s$ states also exhibit clear directional preferences. However, unlike the coupled $1d_1$ states, the individual dot wave function of the $2s$ bonding orbital is oriented perpendicular to the axis, and that of the $2s^*$ antibonding orbital is oriented along the axis. Since the orbitals oriented along the axis have larger wave function overlap between the two dots than those oriented perpendicular to the axis, the $1d_1$ and $2s^*$ orbitals exhibit larger energy shifts than the $1d_1^*$ and $2s$ orbitals as the interdot distance becomes shorter [Fig. 5(c)].

2. Valence band

We plot the hole energies and wave functions of SQD and LCQDs in Figs. 6(a) and 6(b), respectively. Each SQD state is simply labeled by its order (h_1-h_6) due to the mixed characters of hole wave functions. Since holes are less localized in each dot than electrons, due to the smaller band offsets of VB, their energies are more sensitive to the strain anisotropy between the $[110]$ and $[1\bar{1}0]$ directions [as can be seen from Figs. 3(b) and 3(d), the anisotropy of strains exhibit extremum values at the interfaces between InAs and GaAs]. As a consequence, the hole p states of SQD [Fig. 6(a): $\delta_{h3-h2}=8.25$ meV] exhibit much larger splitting than the electron p states [Fig. 5(b): $\delta_{1p2-1p1}=0.212$ meV], and the coupled hole states exhibit larger energy differences between $[110]$ and $[1\bar{1}0]$ LCQDs than the coupled electron states.

There are localized s and p states centered in the coupling region of LCQDs with sufficiently large spatial overlap [LCQDs (-2.96 nm) and LCQDs (-6.15 nm)]. The localized states have much smaller confinement energies than the ground states of other LCQDs. Unlike the localized states in VCQDs, which originate from the strong repulsive potential between the top and bottom dots and the asymmetric strain distributions between the dots, the localized states in LCQDs arise from the strong attractive potential between the dots (Sec. III A). The antibonding orbitals of SQD ground state [h_3 in $[1\bar{1}0]$ LCQDs (-6.15 nm) and h_2 in $[110]$ LCQDs (-6.15 nm)] are localized in each dot due to the node in the coupling region.

In VCQDs, Bester *et al.*[18] reported that the effective barrier felt by the hole states increases upon reduction in the interdot distance, thus lowers the hole energies and leads to form symmetry-broken (heteronuclearlike) states by suppressing tunneling. In contrast, the barrier in LCQDs weakens as the interdot distance decreases, thus raises the energies [Fig. 6(a)] and leads to the symmetric hole states [Fig. 6(b)].

C. Piezoelectric potential

1. Single quantum dot

Figure 7(b) shows the three-dimensional isopotential surfaces of SQD. The red and blue surfaces represent the isos-
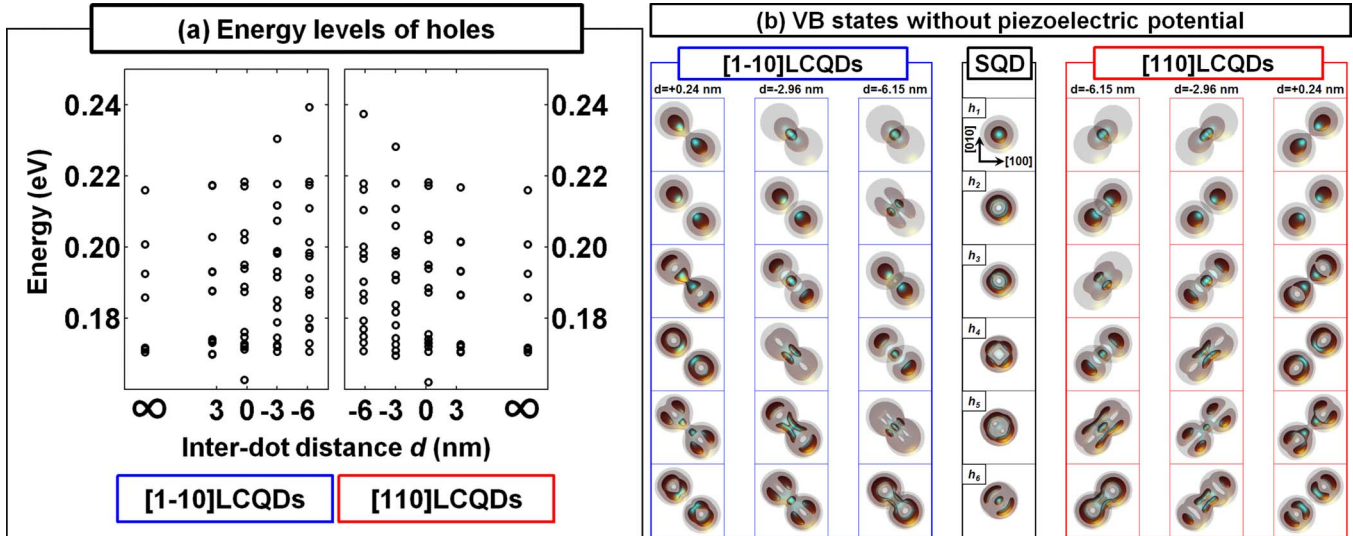
FIG. 6. (Color online) The energy levels of the coupled hole states and the first six hole probability densities in the absence of the piezoelectric potential (or in the presence of the first- and the second-order piezoelectric potentials, see text).

urfaces of the potential values of +45 and −45 mV, respectively. In our coordinate system (Sec. II B), there are negative potentials below the [110] corners and above the [1$\bar{1}$0] corners of SQD and positive potentials below the [1$\bar{1}$0] corners and above the [110] corners [Fig. 7(b)]. To visualize the potential profiles inside the dots, we plot the (001) planes of the piezoelectric potentials 0.565 nm above the base of the dots in Fig. 8(a) and the cross-sections of the potentials along the lines A ((110) planes of [1$\bar{1}$0] LCQDs and SQD and (1$\bar{1}$0) planes of [110] LCQDs) and B (the planes perpendicular to A) in Figs. 8(b) and 8(c), respectively. White contours represent the potential nodes (V_{piezo} =0), black lines in Figs. 8(b) and 8(c) show the outlines of the dots, and the signs in the vicinity of the nodes represent the signs of the potentials. In a dot with shape symmetry higher than D_{4h}, the eight extrema of the piezoelectric potentials located above and below the four corners of the dot have identical magnitudes, thus equally influence the potentials inside the dot. However, since the lens-shaped dot used in this paper lacks of mirror symmetry along the growth direction, the corners of the SQD are mainly affected by the four potential extrema below the dot: the negative potentials at [110] corners and the positive potentials at [1$\bar{1}$0] corners.

In addition, the lacks of symmetry results in uneven distributions between the positive and negative potentials inside the dot: as indicated by the zero potential contours, a larger portion of the dot, including the center, is occupied by a weak positive potential. This can be clearly seen in Fig. 9(a), which shows the number of InAs cells occupied by the potential V_{piezo}. The excessive positive potentials inside the dot (InAs) are compensated by the excessive negative potentials outside the dot (GaAs).

2. Laterally coupled quantum dots

Lateral coupling considerably enhances the potentials located along the axis of coupling: the coupling along the [1$\bar{1}$0] direction [Fig. 7(a)] enhances the positive (negative) potential below (above) the coupling region, and the coupling along the [110] direction [Fig. 7(c)] enhances the negative (positive) potential below (above) the region. On the contrary, the potentials perpendicular to the axis (i.e., the potentials located above and below the [110] ([1$\bar{1}$0]) corners of [1$\bar{1}$0] LCQDs ([110] LCQDs)) are weakened by the coupling. Unlike the hydrostatic strain which changes its sign abruptly at the interfaces between InAs and GaAs, the piezoelectric potential smoothly varies at the interfaces. As a con-
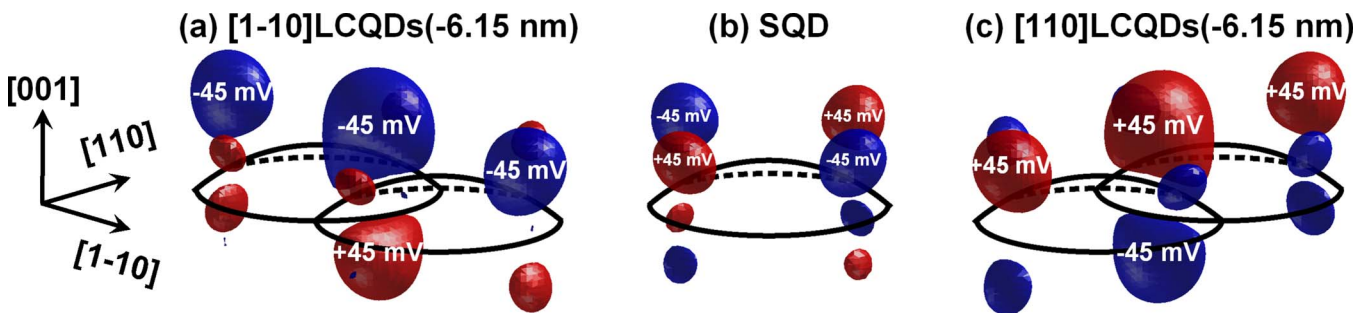
FIG. 7. (Color online) The three-dimensional piezoelectric potential profiles of (a) [1$\bar{1}$0] LCQDs (−6.15 nm), (b) SQD, and (c) [110] LCQDs (−6.15 nm). The red and blue isocontours represent the potential values of +45 and −45 mV, respectively.
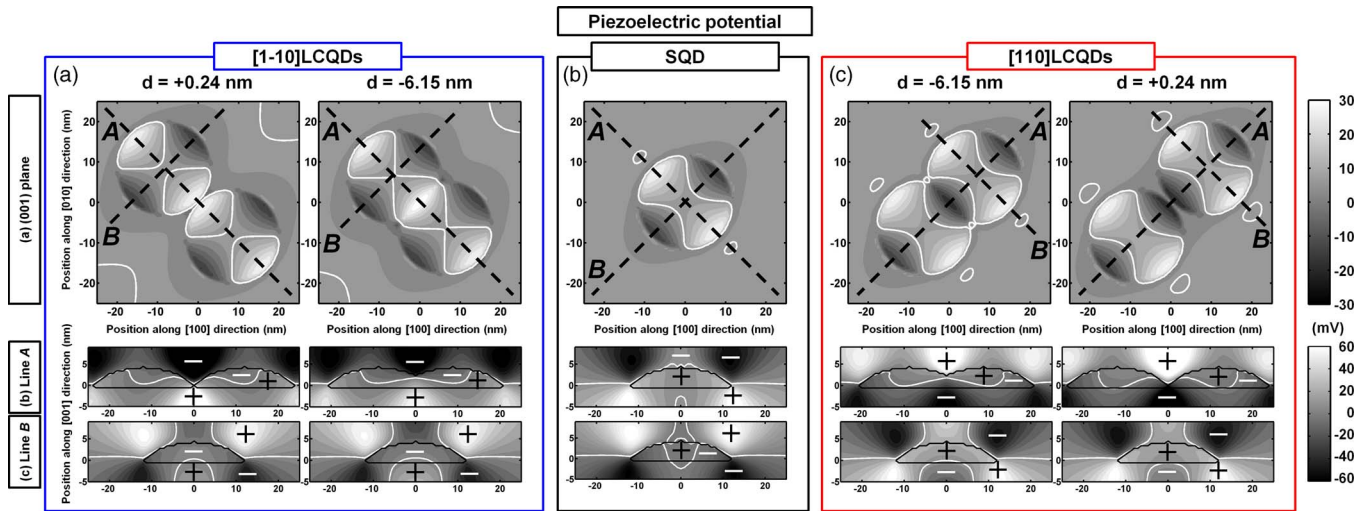
FIG. 8. (Color online) (a) The (001) planes of the piezoelectric potentials 0.565 nm above the base of $[1\bar{1}0]$ LCQDs, SQD, and [110] LCQDs. Lines A represent the $[1\bar{1}0]$ directions in $[1\bar{1}0]$ LCQDs and SQD, and [110] direction in [110] LCQDs, whereas lines B represent the directions perpendicular to lines A. (b) The cross sections of the potentials along the lines A, (c) the cross sections along the lines B. White contours represent the zero potential contours, black lines show the outlines of the dots, and the signs in (b) and (c) represent the signs of the potentials.

sequence, although the piezoelectric potential extrema are located outside the dots, the lateral coupling considerably affects the potential profiles inside the dots. The in-plane profiles and the cross sections of the potentials (Fig. 8) show that the lateral coupling not only enhances the potentials in the coupling region but also modifies the potential profiles in the middle of the dots. For example, the coupling along the $[1\bar{1}0]$ direction enhances the positive potentials in the coupling region, but considerably lowers the potentials in the middle of each dot. Thus, a larger portion of InAs is occupied by negative potentials. Similarly, the coupling along the [110] direction enhances the negative potentials in the coupling region and increases the potentials in the middle of each dot. As a consequence, a larger portion of InAs is occupied by positive potentials. This can be clearly seen in Figs. 9(b) and 9(c). $[1\bar{1}0]$ LCQDs (blue bars with close

circles) exhibits higher positive potential extrema (A in Fig. 9) than [110] LCQDs (red bars with open circles), but most of the cells in $[1\bar{1}0]$ LCQDs have negative potentials (B). On the contrary, [110] LCQDs show lower negative potential extrema (C) than $[1\bar{1}0]$ LCQDs, but most of their cells have positive potentials (D). Since wave functions are not uniformly distributed over the dots, the piezoelectric potential unevenly shifts the energy of each state depending on its spatial distribution (Sec. III D).

D. Electronic structures in the presence of the piezoelectric potential

1. Conduction band

Figures 10(a)–10(c) show the electron energies of SQD and LCQDs calculated from the strains and the piezoelectric
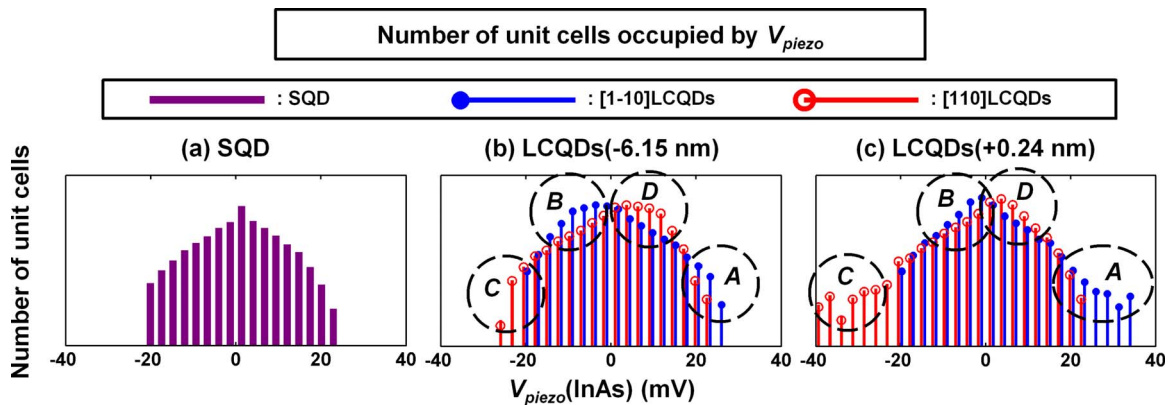
FIG. 9. (Color online) The number of unit cells (y axis: log scale) occupied by the piezoelectric potentials of the magnitude V_{piezo} (x axis: in mV). The red bars in (b) and (c) represent the histograms of [110] LCQDs, and the blue ones do those of $[1\bar{1}0]$ LCQDs. A: the positive potential extremum in $[1\bar{1}0]$ LCQDs, B: the potential occupied by the largest number of unit cells in $[1\bar{1}0]$ LCQDs, C: the negative potential extremum in [110] LCQDs, and D: the potential occupied by the largest number of unit cells in [110] LCQDs.
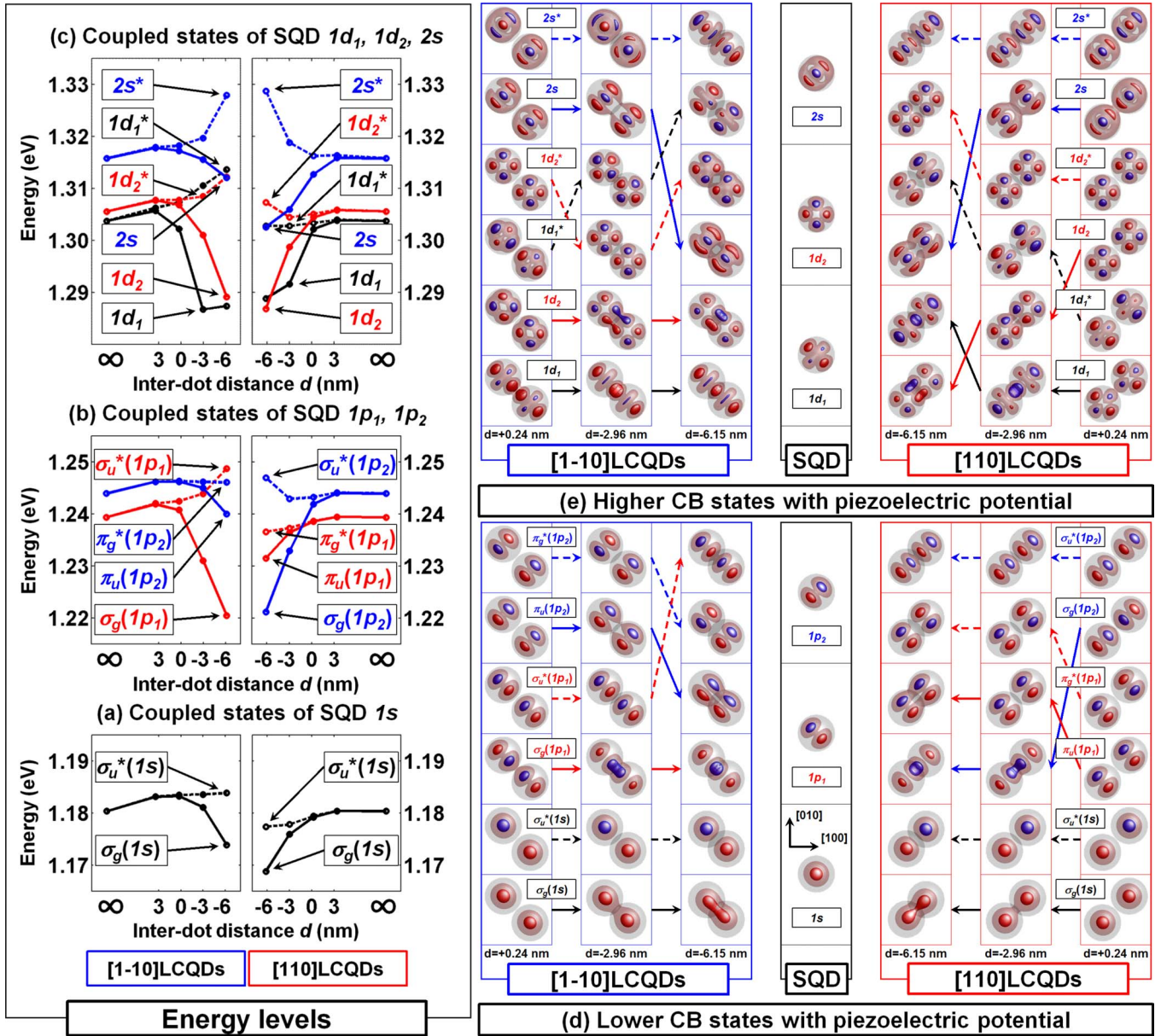
FIG. 10. (Color online) The energy levels of the coupled states originate from the SQD (a) $1s$, (b) $1p_1$ and $1p_2$, and (c) $1d_1$, $1d_2$, and $2s$ states in the presence of the (classical) first-order piezoelectric potential. And the electron probability densities of the coupled states originate from the SQD (d) $1s$, $1p_1$, and $1p_2$, and (e) $1d_1$, $1d_2$, and $2s$ states.

potentials, and Figs. 10(d) and 10(e) show their probability densities. We labeled each state in the same way as in Sec. III B. Note that in the presence of the piezoelectric potential, the first and second excited electron states of SQD are oriented along the $[1\bar{1}0]$ and $[110]$ directions, respectively (i.e., 90° rotated from those in the absence of the potential). We note the following features:

(i) *SQD states and the anisotropy.* Since the SQD ground state is almost localized in the middle of the dot, the state does not exhibit a clear orientation even in the presence of the piezoelectric potential. On the contrary, the excited states show clear preferential directions: the first and third excited states are oriented along the $[1\bar{1}0]$ direction, whereas the second and fifth excited states are oriented along the $[110]$ direction. In addition, as seen from Figs. 10(b) and 10(c), the

splitting between the $1p_1$ and $1p_2$ states ($\delta_{1p2\text{-}1p1}$ =4.56 meV), the $1d_1$ and $1d_2$ states ($\delta_{1d2\text{-}1d1}$=1.83 meV) are considerably increased by the piezoelectric potential compared to those in the absence of the potential.

(ii) *LCQDs states.* The lower molecular orbitals of LCQDs (+3.44 nm) exhibit very small bonding and antibonding splittings due to their small wave function overlaps. However, the energy splitting considerably increases as the interdot distance decreases [LCQDs (+0.24 nm) to LCQDs (−6.15 nm) in Fig. 10]. The SQD $1p_1$ states form σ (π) orbitals with a large (small) splitting in $[1\bar{1}0]$ LCQDs ($[110]$ LCQDs), whereas the SQD $1p_2$ states form π (σ) orbitals with a small (large) splitting in $[1\bar{1}0]$ LCQDs ($[110]$ LCQDs). The electron probability densities in the coupling region increase by the coupling along the $[1\bar{1}0]$ direction

[clearly can be seen from $\sigma_g(1s)$ in Fig. 10(d)] since the coupling enhances the positive piezoelectric potential in the region. The opposite is true for the coupling along the [110] direction. As a consequence, the degeneracy between the σ (and π) orbitals of $[1\bar{1}0]$ and [110] LCQDs, which is observed in the absence of the piezoelectric potential (Sec. III B and Fig. 5), is lifted by the difference between the degrees of spatial overlaps caused by the piezoelectric potentials. The σ orbitals of the SQD $1s$ states $[\sigma_g(1s)$ and $\sigma_u^*(1s)]$ in $[1\bar{1}0]$ LCQDs (−6.15 nm) exhibit a larger bonding-antibonding splitting (9.99 meV) than those in [110] LCQDs (−6.15 nm) (8.57 meV) due to the larger spatial overlap between the wave functions in $[1\bar{1}0]$ LCQDs than those in [110] LCQDs. Similarly, both the σ and π orbitals of the SQD $1p_1$ and $1p_2$ states in $[1\bar{1}0]$ LCQDs (−6.15 nm) [28.3 meV splitting between $\sigma_g(1p_1)$ and $\sigma_u^*(1p_1)$, and 6.13 meV splitting between $\pi_u(1p_2)$ and $\pi_g^*(1p_2)$] show larger splitting than those in [110] LCQDs (−6.15 nm) (25.8 meV splitting for σ orbitals and 5.06 meV for π orbitals).

As expected from the distributions of the piezoelectric potentials (Figs. 8 and 9), the potentials unevenly shift the energy of each state depending on its spatial distribution. In $[1\bar{1}0]$ LCQDs, the potential raises the energies of $\sigma(1s)$ and $\pi(1p)$ orbitals (Fig. 10) since most of their electron probabilities are located in the middle and [110] corners of each dot, which have negative piezoelectric potentials (Fig. 8). On the contrary, the energies of $\sigma(1p)$ orbitals are lowered by the positive potentials in $[1\bar{1}0]$ corners, but the amounts of the shifts are much smaller than those of $\sigma(1s)$ and $\pi(1p)$. This is because $\sigma(1p)$ orbitals have still sizable electron probabilities in the regions with negative potentials [as shown by the outer probability isosurfaces in Fig. 10(d)] since the coupling along the $[1\bar{1}0]$ direction increases the number of unit cells occupied by the negative potentials near the middle of each dot (Figs. 8 and 9). Since the increment in the energies by the negative potentials partially compensate the shifts by the positive potentials in $[1\bar{1}0]$ corners, the energies of $\sigma(1p)$ orbitals exhibit much smaller shifts than those of $\sigma(1s)$ and $\pi(1p)$. Similarly, the coupling along the [110] direction lowers the energies of $\sigma(1s)$ and $\pi(1p)$ orbitals by the positive potentials in the middle and $[1\bar{1}0]$ corners of each dot. Although a larger electron probabilities of $\sigma(1p)$ orbitals are found in [110] corners of each dot, which have negative potentials, the $\sigma(1p)$ orbitals exhibit very weak decrement in the energies due to the strong positive potentials in the middle of each dot (Figs. 8 and 9). As a consequence, the lateral coupling along the $[1\bar{1}0]$ direction reduces the splitting between $\sigma(1s)$ and $\sigma(1p)$ orbitals, whereas the coupling along the [110] direction increases the splitting. In addition, also the differences between the probability distributions of $\sigma(1s)$ and $\pi(1p)$ orbitals give rise to (small) uneven shifts of the energies of those states: the coupling along the $[1\bar{1}0]$ direction slightly increases the splitting between $\sigma(1s)$ and $\pi(1p)$ orbitals, whereas the coupling along the [110] direction decreases the splitting.

(iii) *Higher excited state.* Similarly to Sec. III B, the coupled $1d_1$ (and $2s$) states exhibit large deformations from the initial probability distributions of SQD states. For example, as the distance between the dots decreases, the $2s^*$ orbital of $[1\bar{1}0]$ LCQDs changes its orientation from [110] ($[1\bar{1}0]$ LCQDs (+0.24 nm)) to $[1\bar{1}0]$ direction ($[1\bar{1}0]$ LCQDs (−6.15 nm)). The $2s^*$ orbital in $[1\bar{1}0]$ LCQDs (−2.96 nm) exhibits an intermediate state. In spite of the large deformations, the angular momentum of individual dot is still preserved in the coupled states: the coupled $2s$ states have large s orbital characters (e.g., the $1d_1$, $1d_2$, $2s$, $1d_2^*$, $1d_1^*$, and $2s^*$ orbitals of $[1\bar{1}0]$ LCQDs (−6.15 nm) have 1.54, 0.01, 16.2, 2.83, 5.41, and 32.2% s characters), whereas the coupled $1d_1$ (91.7% d character) and $1d_2$ (93.4% d character) states have large d orbital characters.

2. Valence band

We plot the hole energies and wave functions of the SQD and LCQDs in Fig. 11. Most of the SQD hole states show clear elongation along the [110] directions due to the positive piezoelectric potentials in the [110] corners. In addition, the piezoelectric potential increases the energy splitting between the SQD p states: h_2 and h_3 states in the presence of the potential exhibit a splitting of 9.87 meV, whereas those in the absence of the potential show a splitting of 8.25 meV. Similarly to Sec. III B, there are localized s and p states in the coupling region due to the strong confinement potentials in the region. However, the localized s states of $[1\bar{1}0]$ LCQDs ([110] LCQDs) are less (more) confined in the coupling region than those in the absence of the piezoelectric potential due to the strong positive (negative) potential at the region. Thus, [110] LCQDs exhibits a larger energy splitting between the first two hole orbitals than $[1\bar{1}0]$ LCQDs. Similarly to Sec. III B, the antibonding orbitals of SQD ground state (h_2 in $[1\bar{1}0]$ LCQDs (−6.15 nm) and h_3 in [110] LCQDs (−6.15 nm)) are localized in each dot due to the node in the coupling region. As expected from the number of unit cells occupied by the positive and negative potentials (Figs. 8 and 9), the overall hole energies, except those of the localized ones, are raises (lowered) by the coupling along the $[1\bar{1}0]$ ([110]) directions.

E. Optical properties

1. Intraconduction band spectra

We plot the intraband absorption spectra in the absence and presence of the piezoelectric potential in Figs. 12(a) and 12(b), respectively. The length of each peak represents the transition oscillator strength, and the blue peaks exhibit the transitions polarized along the $[1\bar{1}0]$ direction, whereas the red ones do those along the [110] direction. To simplify the analysis, we plot the peaks related to the $1s$, $1p_1$, and $1p_2$ states of SQD and their coupled states only (i.e., no higher excited states such as the $1d_1$, $1d_2$, or $2s$ states are included).

The two peaks of the SQD ($d=\infty$) are associated with the transition between the $1p_1$ and $1s$ states and that between the $1p_2$ and $1s$ states. In the absence of the piezoelectric potential, those two peaks are almost degenerated due to the small
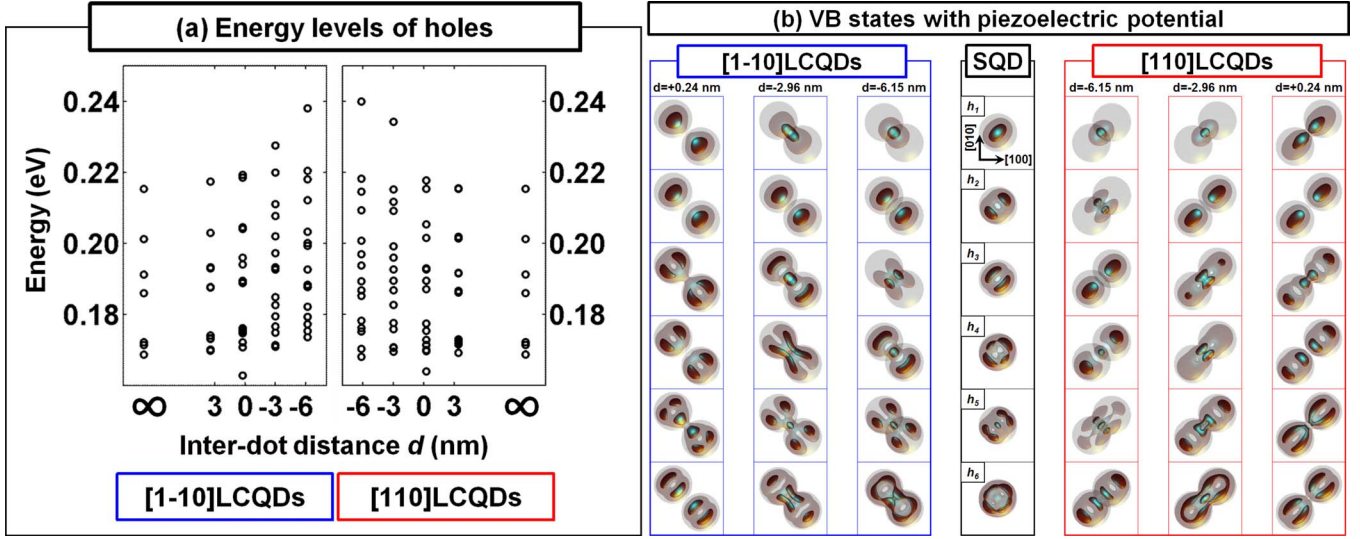
FIG. 11. (Color online) (a) The energy levels of the coupled hole states and (b) the first six hole probability densities in the presence of the (classical) first-order piezoelectric potential.

splitting between the two p states. As the interdot distance shrinks, four peaks $[\sigma_g(1p_{2(1)})-\sigma_u^*(1s), \pi_g^*(1p_{1(2)})-\sigma_u^*(1s), \pi_u(1p_{1(2)})-\sigma_g(1s),$ and $\sigma_u^*(1p_{2(1)})-\sigma_g(1s)]$ arise from the transitions between the two coupled s states $(1s, 1s^*)$ and the four coupled p states $(1p_1, 1p_1^*, 1p_2,$ and $1p_2^*)$. Here, $\sigma_g(1p_{2(1)})-\sigma_u^*(1s)$ denotes the two transitions: $\sigma_g(1p_2)-\sigma_u^*(1s)$ of $[1\bar{1}0]$ LCQDs and $\sigma_g(1p_1)-\sigma_u^*(1s)$ of $[110]$ LCQDs. The other transitions are forbidden by the selection rules, which will be described in this section. The absorption to the $\sigma(1p)$ orbitals $[\sigma_g(1p_{2(1)})-\sigma_u^*(1s)$ and $\sigma_u^*(1p_{2(1)})-\sigma_g(1s)$: designated as "group sigma" in Fig. 12] exhibit larger splitting than those to the $\pi(1p)$ orbitals $[\pi_g^*(1p_{1(2)})-\sigma^*(1s)$ and $\pi_u(1p_{1(2)})-\sigma(1s)$: "group pi"]. This is because (i) the π orbitals (in group pi) themselves have a smaller bonding-antibonding splitting energy than the σ orbitals (in group sigma) and (ii) the energy splitting between the two transitions in group pi is the difference between the bonding-antibonding splitting of the s and p orbitals $(\delta_{\pi^*(1p)-\pi(1p)} - \delta_{\sigma^*(1s)-\sigma(1s)})$, whereas the splitting between the two transitions in group sigma is the sum of them $(\delta_{\sigma^*(1p)-\sigma(1p)} + \delta_{\sigma^*(1s)-\sigma(1s)})$. The two transitions in group pi have similar oscillator strengths independent to the interdot distances. On the contrary, in group sigma, the transition with a lower energy $[\sigma_g(1p_{2(1)})-\sigma_u^*(1s)]$ exhibits a stronger oscillator strength as the interdot distance shrinks, whereas that with a higher energy $[\sigma_u^*(1p_{2(1)})-\sigma_g(1s)]$ almost vanishes.

As the deformation of individual dot wave function becomes larger, the transitions between the bonding and antibonding states of SQD s state (and between the coupled p states) also exhibits a stronger transition oscillator strength with a larger transition energy. For example, the $\sigma_u^*(1p_{2(1)})-\sigma_g(1p_{2(1)})$ transition exhibits a sizable oscillator strength comparable to those in groups sigma and pi and even exceeds them in highly overlapped LCQDs.

The intraband spectra of both $[1\bar{1}0]$ LCQDs and $[110]$ LCQDs exhibit almost the same transition energies and oscillator strengths since the energy levels and probability dis-

tributions along the coupling axis are less sensitive to the lateral coupling directions (Fig. 5). However, since each intraband transition is exclusively activated by only one of the $[110]$ and $[1\bar{1}0]$ polarized light, and most transitions, except group pi, are polarized along the axis passing through the dots, the coupling directions can be clearly distinguished by the polarization of each transition. One of the merits of pseudoquantum numbers is that it provides clear information on the selection rule and polarization of each transition. As indicated by Schliwa *et al.*,[28] the necessary condition for the nonvanishing oscillator strength for the transitions between the two electron states, $|a\rangle=|n_1,n_2,n_3\rangle$ and $|b\rangle=|n_1',n_2',n_3'\rangle$, is that at least one of the resulting numbers n_1-n_1', n_2-n_2', or n_3-n_3' is odd. In addition, the transition is $[110]$ ($[1\bar{1}0]$) polarized if the expression n_1-n_1' (n_2-n_2') is an odd number. The same rule can be applied to the transitions between the coupled states by defining the pseudoquantum number of molecular orbital in the same way as that of SQD state: i.e., the number of nodes along the $[110]$, $[1\bar{1}0]$, and $[001]$ directions of the molecular orbital. In this definition, the pseudoquantum numbers of $\sigma_g(1s)$, $\sigma_u^*(1s)$, $\sigma_g(1p_2)$, $\pi_u(1p_1)$, $\pi_g^*(1p_1)$, and $\sigma_u^*(1p_2)$ in $[1\bar{1}0]$ LCQDs (-6.15 nm) (Fig. 5) are $|0,0,0\rangle$, $|0,1,0\rangle$, $|0,2,0\rangle$, $|1,0,0\rangle$, $|1,1,0\rangle$, and $|0,3,0\rangle$. The observed seven transitions in Fig. 12(a) obey the selection rule, and five of them $(|1,1,0\rangle-|1,0,0\rangle$, $|0,1,0\rangle-|0,0,0\rangle$, $|0,3,0\rangle-|0,2,0\rangle$, $|0,2,0\rangle-|0,1,0\rangle$, and $|0,3,0\rangle-|0,0,0\rangle)$ are polarized along the $[1\bar{1}0]$ directions, whereas the others $(|1,1,0\rangle-|0,1,0\rangle$ and $|1,0,0\rangle-|0,0,0\rangle)$ are polarized along the $[110]$ directions. In addition, only the transitions between g and u are allowed similar to the selection rule of diatomic molecules. Neither the transitions between g and g^* nor u and u^* are allowed.

Figure 12(b) shows the intraband transition spectra in the presence of the piezoelectric potential. The C_{2v} symmetry of the piezoelectric potential lifts the degeneracy of the two SQD intraband transitions by 4.56 meV. The order of the transitions in LCQDs and their relative intensity remain un-
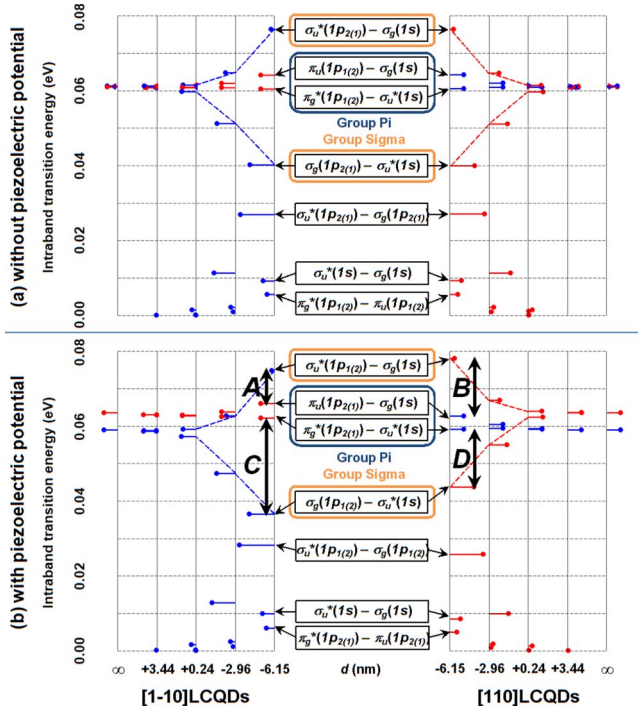
FIG. 12. (Color online) Intraconduction band transition spectra in the (a) absence and (b) presence of the piezoelectric potential. The red lines represent the transitions activated by [110] polarized light, and the blue ones do those activated by $[1\bar{1}0]$ polarized light. Group sigma represents the absorptions from the coupled s states to $\sigma(1p)$ orbitals, and group pi represents those from the coupled s states to $\pi(1p)$ orbitals. A and B represent the splitting between the two transitions from the bonding s orbitals $[\sigma_g(1s)]$ to the two coupled p orbitals in $[1\bar{1}0]$ and [110] LCQDs, respectively, whereas C and D represent the splitting between the two transitions from the antibonding s orbitals $[\sigma_u^*(1s)]$ to the two coupled p orbitals in $[1\bar{1}0]$ and [110] LCQDs, respectively.

changed except the commutation of the $1p_1$ and $1p_2$ states: as shown in Fig. 10, the first (second) excited electron state of SQD is oriented along the $[1\bar{1}0]$ ([110]) direction, i.e., 90° rotated from those in the absence of the potential. As shown above (Sec. III D), since the positive (negative) piezoelectric potentials in the coupling regions of $[1\bar{1}0]$ LCQDs ([110] LCQDs) enhance (reduce) the wave function overlap in the regions, the group sigma in $[1\bar{1}0]$ LCQDs exhibits a larger splitting than that in [110] LCQDs.

As discussed in Sec. III D, the piezoelectric potential unevenly shifts the energies of $\sigma(1s)$, $\sigma(1p)$, and $\pi(1p)$ orbitals of $[1\bar{1}0]$ LCQDs and [110] LCQDs depending on their spatial distributions: the lateral coupling along the $[1\bar{1}0]$ direction reduces the splitting between $\sigma(1s)$ and $\sigma(1p)$ orbitals and slightly increases the splitting between $\sigma(1s)$ and $\pi(1p)$ orbitals, whereas the coupling along the [110] direction increases the splitting between $\sigma(1s)$ and $\sigma(1p)$ orbitals and slightly decreases the splitting between $\sigma(1s)$ and $\pi(1p)$ orbitals. As a consequence, the piezoelectric potential considerably changes the energy splitting between the transitions to the coupled p orbitals. For example, the energy splitting be-

tween the two transitions from the bonding s orbitals $[\sigma_g(1s)]$ to the two coupled p orbitals $\{\pi_u[1p_{2(1)}]\}$ and $\{\sigma_u^*[1p_{1(2)}]\}$ in $[1\bar{1}0]$ LCQDs is decreased by the piezoelectric potential [A in Fig. 12: 1.10 and 8.76 meV splitting for the interdot distances (d) of −2.96 and −6.15 nm, respectively], whereas the splitting in [110] LCQDs is increased by the potential (B: 6.47 and 15.5 meV splitting for d of −2.96 and −6.15 nm, respectively). On the contrary, the energy splitting between the two transitions from the antibonding s orbitals $[\sigma_g(1p_{1(2)}) - \sigma_u^*(1s)$ and $\pi_g^*(1p_{2(1)}) - \sigma_u^*(1s)]$ in $[1\bar{1}0]$ LCQDs is increased by potential (C: 15.1 and 25.6 meV splitting, respectively), and the splitting in [110] LCQDs is decreased by the potential (D: 4.38 and 15.4 meV splitting, respectively).

2. Interband spectra

Figure 13 shows the single-exciton energies of SQD ($d = \infty$) and LCQDs calculated by using the configuration interaction (CI) method.[43] The CI bases (configurations) of SQD are built from six single-electron states and six single-hole states wave functions. The number of single-particle states are doubled in LCQDs to represent the bonding and antibonding states. Since each single-particle energy level is at least doubly degenerate due to the time-reversal symmetry,[30,44] each configuration has a minimum dimension of four.[45] Vertical dotted lines show the excitonic energy levels. The red solid lines show the absorption spectra (oscillator strength) with [110] polarized light, whereas the blue dotted lines show those with $[1\bar{1}0]$ polarized light. The large oscillator strength indicates that the exciton is optically active (bright exciton), whereas the small one indicates that the exciton is optically dark. Each peak is labeled by the configuration from which they originate. $\sigma_u^*(1s) - h_{2(3)}$ denotes the two transitions: $\sigma_u^*(1s) - h_2$ of $[1\bar{1}0]$ LCQDs and $\sigma_u^*(1s) - h_3$ of [110] LCQDs.

Figure 13(a) shows the excitonic energies in the absence of the piezoelectric potential. The exciton ground-state absorption spectrum (s channel) of SQD exhibits a relatively small anisotropy between the oscillator strength of [110] and $[1\bar{1}0]$ polarized light. The transitions between $1s$-h_2, $1s$-h_3, $1p_1$-h_1, and $1p_2$-h_1 (range from 0.965 to 1.01 eV) are almost forbidden by the different symmetry of the electron and hole wave functions.

The four lowest-energy excitons of LCQDs, except LCQDs (−6.15 nm), mainly originate from the configurations built from the electron and hole $\sigma_g(1s)$ and $\sigma_u^*(1s)$ orbitals (s channel). In both $[1\bar{1}0]$ LCQDs and [110] LCQDs the lowest exciton energies decrease as the interdot distance shrinks. The large redshifts of the lowest exciton energies in both LCQDs (−2.96 nm) and LCQDs (−6.15 nm) are mainly because of the localized hole states which have very small confinement energies (Fig. 6).

In LCQDs (−6.15 nm), the exciton energy of $\sigma_g(1s) - h_4$ becomes lower than that of $\sigma_u(1s) - h_{3(2)}$. Although the interband transitions are activated by both the [110] and $[1\bar{1}0]$ polarized light, lateral coupling of QDs enhances the anisotropy between the light polarized along the two directions:
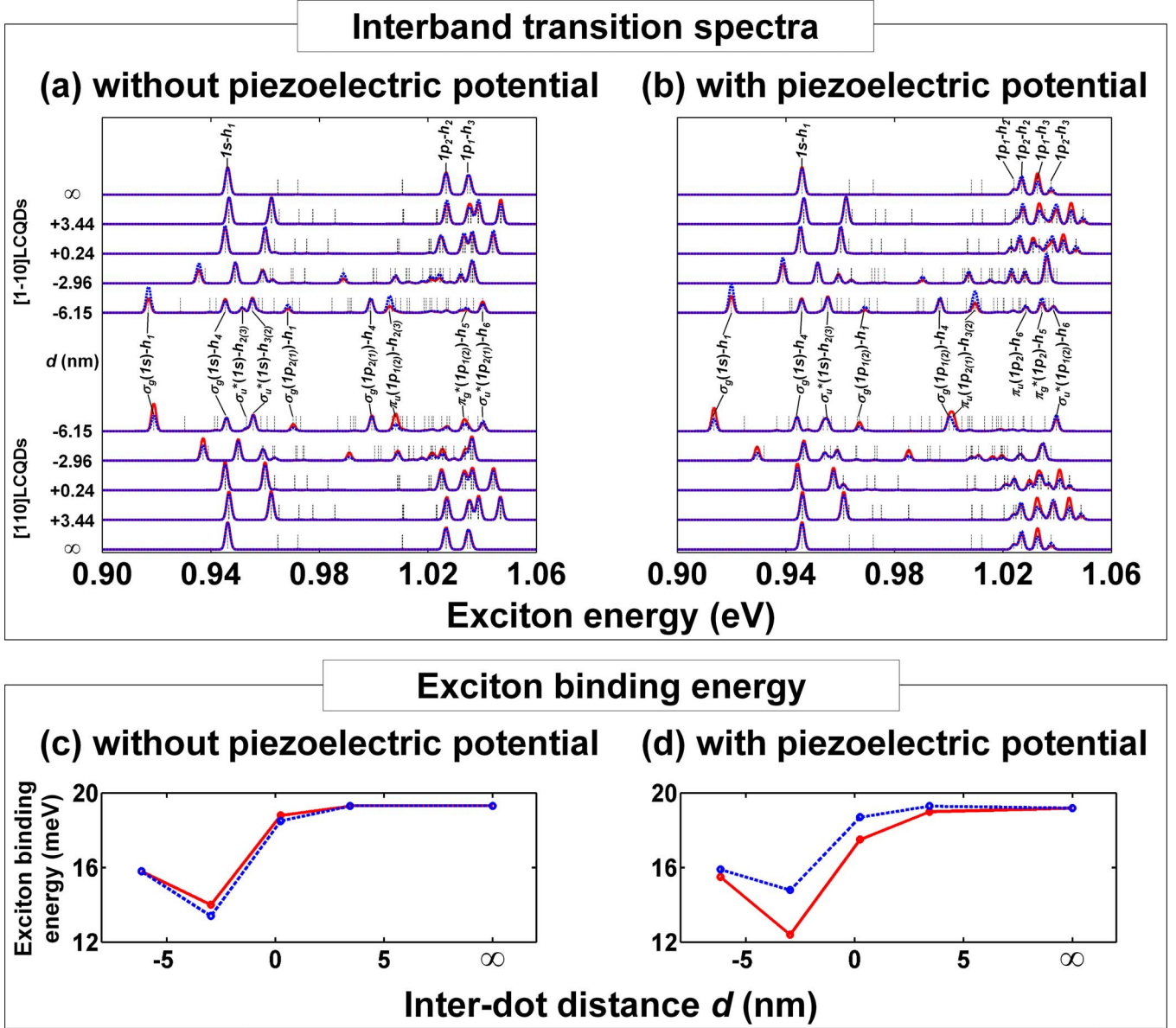
FIG. 13. (Color online) Interband transition spectra calculated by using the CI method in the (a) absence and (b) presence of the piezoelectric potential. Vertical dotted lines show the excitonic energy levels. The red solid lines represent the transitions activated by [110] polarized light, and the blue dotted ones do those activated by [1$\bar{1}$0] polarized light. Each peak is labeled by the configuration from which they originate. Exciton binding energy of the lowest exciton as a function of interdot distance in the (c) absence and (d) presence of the piezoelectric potential. The red solid lines represent the exciton binding energies of [110] LCQDs, and the blue dotted ones do those of [1$\bar{1}$0] LCQDs.

the lowest excitonic peaks of LCQDs exhibit twice larger oscillator strength to the light polarized along the coupling directions of LCQDs.

We plot the excitonic energies in the presence of the piezoelectric potential in Fig. 13(b). The exciton ground-state absorption spectrum (*s* channel) of SQD exhibits a relatively small anisotropy between the oscillator strength of [110] and [1$\bar{1}$0] polarized light, whereas the transition in *p* channel, $1p_2$-h_2 ($1p_1$-h_3) shows larger oscillator strength to [1$\bar{1}$0] ([110]) polarized light than [110] ([1$\bar{1}$0]) polarized one. The peaks in *p* channel of SQD spectra have the same order to those of Fig. 19 (a1) in Schliwa *et al.*[28] since the splitting

between the hole states h_2 and h_3 is larger than that between the electron states $1p_1$ and $1p_2$ (note that *E*000, *E*010, *E*100, *H*0, *H*1, and *H*2 in Ref. 28 correspond to $1s$, $1p_1$, $1p_2$, h_1, h_2, and h_3 in this paper). However, the splitting between $1p_1$-h_2 and $1p_2$-h_2, $1p_1$-h_3 and $1p_2$-h_3 of our dot is much larger than that of Ref. 28 due to the absence of the second-order piezoelectric potential and the larger dot geometry. Similarly to the spectra in the absence of the piezoelectric potential, lateral coupling of QDs enhances the polarization anisotropy of the lowest excitonic peaks.

In both [1$\bar{1}$0] and [110] LCQDs, the lowest exciton energy decreases as the interdot distance shrinks. However, the

magnitude of the shift is different along the $[110]$ and $[1\bar{1}0]$ coupling directions. This is mainly because the lowest CB orbitals $[\sigma_g(1s)]$ are localized in each dot, whereas the highest VB orbitals (h_1) are localized in the coupling region. Since the piezoelectric potentials in the coupling region of LCQDs have opposite signs to those in the middle of each dot, as shown in Sec. III C, the lowest CB orbitals of $[1\bar{1}0]$ LCQDs have larger energies than those of $[110]$ LCQDs, whereas the highest VB orbitals of $[1\bar{1}0]$ LCQDs have lower energies than those of $[110]$ LCQDs. As a consequence, the lowest exciton energy of $[110]$ LCQDs exhibits larger shift than that of $[1\bar{1}0]$ LCQDs: $[110]$ LCQDs peaks exhibit 1.7, 16.5, and 32.4 meV shifts from SQD peak for interdot distances of 0.24, −2.96, and −6.15 nm, whereas $[1\bar{1}0]$ LCQDs peaks show 0.6, 7.1, and 26.0 meV shift from SQD peak.

For the same reason, the splitting between the two lowest optically active states of $[110]$ LCQDs exhibit larger energy splitting than that of $[1\bar{1}0]$ LCQDs when the interdot distance becomes sufficiently short. In LCQDs with small overlap between the dots, the two peaks of $[1\bar{1}0]$ LCQDs show slightly larger splitting than those of $[110]$ LCQDs: 0.33 meV larger splitting in LCQDs (+3.44 nm) and 1.53 meV larger splitting in LCQDs (+0.24 nm). However, as the interdot distance shrinks, the peak splitting of $[110]$ LCQDs becomes larger than that of $[1\bar{1}0]$ LCQDs: 4.22 meV larger splitting in LCQDs (+3.44 nm) and 5.24 meV larger splitting in LCQDs (+0.24 nm). This can also be explained by the piezoelectric potential profiles and the probability distributions of holes. In LCQDs (−2.96 nm) and LCQDs (−6.15 nm), the highest hole $\sigma_g(1s)$ orbitals are localized in the coupling region, whereas the hole $\sigma_u^*(1s)$ orbitals are localized in each dot. Thus, the piezoelectric potential of $[1\bar{1}0]$ LCQDs lowers the energy of $\sigma_g(1s)$ orbital and raises that of $\sigma_u^*(1s)$ orbitals, whereas the potential of $[110]$ LCQDs raises the energy of $\sigma_g(1s)$ orbital and lowers that of $\sigma_u^*(1s)$ orbitals. As a consequence, as the interdot distance becomes sufficiently close to form the hole ground states localized in the coupling region, the splitting between the two lowest absorption peaks of $[110]$ LCQDs exhibit larger energy splitting than that of $[1\bar{1}0]$ LCQDs. As the interdot distance decreases, the number of p channels which show large oscillator strengths decreases.

We plot the exciton binding energy of the lowest exciton in the absence and presence of the piezoelectric potential in Figs. 13(c) and 13(d), respectively. The exciton binding energy slightly decreases as the interdot distance shrinks from infinite to 0.24 nm. This is because the hole ground state of LCQDs (+0.24 nm) is biased toward the coupled region, whereas the electron ground state is located at the center of each dot (Figs. 5, 6, 10, and 11). As a consequence, the spatial electron-hole overlap of LCQDs (+0.24 nm) is a little smaller than that of SQD and LCQDs (+3.44 nm), resulting in a smaller exciton binding energy. The exciton binding energy of LCQDs (−2.96 nm) exhibits much smaller value (more than 3.9 meV) than that of LCQDs (+0.24 nm) since the formation of localized hole state in LCQDs (−2.96 nm) considerably decreases the electron-

hole overlap (Figs. 6 and 11). As the interdot distance decreases to −6.15 nm, the exciton binding energy increases since not only the hole state but also the electron state has a finite probability density at the coupled region. In the absence of the piezoelectric potential, there is little difference (less than 0.6 meV) between the exciton binding energies of $[1\bar{1}0]$ and $[110]$ LCQDs. However, in the presence of the piezoelectric potential, $[110]$ LCQDs has smaller exciton binding energy than $[1\bar{1}0]$ LCQDs. This is because the negative piezoelectric potential in the coupled region of $[110]$ LCQDs (Fig. 8) repels electrons (Fig. 10) and attracts holes (Fig. 11), resulting in a smaller electron-hole overlap.

IV. CONCLUSION

We investigated the electronic and optical properties of self-assembled LCQDs by varying the direction of coupling ($[110]$ and $[1\bar{1}0]$) and the interdot distance. We note the following features. (i) The compressive (biaxial) strain of InAs near the coupling region weakens (increases) as the interdot distance is reduced. The strain-modified band-edge potentials show that the coupling region provides a stronger confinement for both electrons and holes than the center of each dot. (ii) In LCQDs, unlike VCQDs in which both the $1p_1$ and $1p_2$ states form π molecular orbitals, the SQD $1p$ states oriented along the axis passing through the two dots form σ orbitals with large bonding-antibonding splitting, whereas the other $1p$ states oriented perpendicular to the axis form π orbitals with small splitting. (iii) Localized hole s and p states are found in the LCQDs with sufficiently large spatial overlap. Unlike the localized states of VCQDs, which originate from the asymmetric strain distributions between the top and bottom dots, the localized states in LCQDs arise from the strong confinement of HH in the coupling region, thus each state is centered in the coupling region. (iv) In the absence of the piezoelectric potential, the electron coupled states exhibit very small anisotropy between the $[1\bar{1}0]$ and $[110]$ LCQDs, whereas the hole-coupled states show larger anisotropy since they are less localized in each dot than electrons. (v) The lateral coupling along the $[110]$ ($[1\bar{1}0]$) direction enhances the negative (positive) piezoelectric potential in the coupling region and lowers (raises) the potential in the middle of each dot. Since wave functions are not uniformly distributed over the dots, the piezoelectric potential unevenly shifts the energy of each state depending on its spatial distribution and lifts the degeneracy between the electron energies of $[1\bar{1}0]$ and $[110]$ LCQDs. In $[1\bar{1}0]$ LCQDs, the potential raises the energies of $\sigma(1s)$ and $\pi(1p)$ orbitals and slightly lowers those of $\sigma(1p)$ orbitals. On the contrary, the coupling along the $[110]$ direction lowers the energies of $\sigma(1s)$ and $\pi(1p)$ orbitals and slightly lowers those of $\sigma(1p)$ orbitals. (vi) In the presence of the piezoelectric potential, the energy splitting of the transitions to p states in SQD is 4.56 meV. The potential decreases the splitting between the two transitions from the bonding s orbitals $[\sigma_g(1s)]$ to the two coupled p orbitals in $[1\bar{1}0]$ LCQDs and increases the splitting in $[110]$ LCQDs. Similarly, the potential increases the splitting be-

tween the transitions from the antibonding *s* orbitals $[\sigma_u^*(1s)]$ to the two coupled *p* orbitals in $[1\bar{1}0]$ LCQDs and decreases the splitting in $[110]$ LCQDs. (vii) The coupling direction is clearly distinguishable by the polarization of intraband transitions since most transitions are polarized along the axis passing through the two dots. (viii) Pseudoquantum numbers (the number of nodes along the $[110]$, $[1\bar{1}0]$, and $[001]$ directions) of the molecular orbitals provide clear information for the selection rule and the polarization of each transition. (ix) Lateral coupling enhances the polarization anisotropy of interband absorption spectra. (x) Due to the nonuniform piezoelectric potential distributions and the localized hole states, $[110]$ LCQDs (-2.96 nm) and $[110]$ LCQDs (-6.15 nm) exhibit larger redshift of the lowest exciton energies and larger splitting between the two lowest optically active states than $[1\bar{1}0]$ LCQDs (-2.96 nm) and $[1\bar{1}0]$ LCQDs (-6.15 nm). (xi) Since the negative piezoelectric potential in the coupled region of $[110]$ LCQDs reduces the spatial electron-hole overlap, $[110]$ LCQDs has smaller exciton binding energy than $[1\bar{1}0]$ LCQDs.

ACKNOWLEDGMENTS

[1] G. Schedelbeck, W. Wegscheider, M. Bichler, and G. Abstreiter, Science **278**, 1792 (1997).

[2] M. Bayer, P. Hawrylak, K. Hinzer, S. Fafard, M. Korkusinski, Z. R. Wasilewski, O. Stern, and A. Forchel, Science **291**, 451 (2001).

[3] F. R. Waugh, M. J. Berry, D. J. Mar, R. M. Westervelt, K. L. Campman, and A. C. Gossard, Phys. Rev. Lett. **75**, 705 (1995).

[4] G. J. Beirne, C. Hermannstadter, L. Wang, A. Rastelli, O. G. Schmidt, and P. Michler, Phys. Rev. Lett. **96**, 137401 (2006).

[5] Y.-J. Yu, H. Noh, G. S. Jeon, H.-R. Noh, Y. Arakawa, and W. Jhe, Appl. Phys. Lett. **91**, 041117 (2007).

[6] A. J. Markvoort, P. A. J. Hilbers, and R. Pino, J. Phys.: Condens. Matter **15**, 6977 (2003).

[7] R. M. Abolfath and P. Hawrylak, J. Chem. Phys. **125**, 034707 (2006).

[8] B. Szafran and F. M. Peeters, Phys. Rev. B **76**, 195442 (2007).

[9] S.-S. Li and J.-B. Xia, Chin. Phys. **16**, 1 (2007).

[10] J. H. Lee, Z. M. Wang, N. W. Strom, Y. I. Mazur, and G. J. Salamo, Appl. Phys. Lett. **89**, 202101 (2006).

[11] J. H. Lee, K. Sablon, Z. M. Wang, and G. J. Salamo, J. Appl. Phys. **103**, 054301 (2008).

[12] L. R. C. Fonseca, J. L. Jimenez, J. P. Leburton, and R. M. Martin, Phys. Rev. B **57**, 4017 (1998).

[13] O. Stier, M. Grundmann, and D. Bimberg, Phys. Rev. B **59**, 5688 (1999).

[14] G. Bester, X. Wu, D. Vanderbilt, and A. Zunger, Phys. Rev. Lett. **96**, 187602 (2006).

[15] L. He, G. Bester, and A. Zunger, Phys. Rev. B **72**, 081311(R) (2005).

[16] S. Nagaraja, J.-P. Leburton, and R. M. Martin, Phys. Rev. B **60**, 8759 (1999).

[17] W. Sheng and J.-P. Leburton, Appl. Phys. Lett. **81**, 4449 (2002).

[18] G. Bester, A. Zunger, and J. Shumway, Phys. Rev. B **71**, 075325 (2005).

[19] P. N. Keating, Phys. Rev. **145**, 637 (1966).

[20] R. M. Martin, Phys. Rev. B **1**, 4005 (1970).

[21] W. H. Press, S. A. Teukolsky, W. T. Vetterling, and B. P. Flannery, *Numerical Recipes in C 2nd Edition: The Art of Scientific Computing* (Cambridge University Press, New York, 1992).

[22] C. Pryor, J. Kim, L. W. Wang, A. J. Williamson, and A. Zunger, J. Appl. Phys. **83**, 2548 (1998).

[23] G. Bester and A. Zunger, Phys. Rev. B **71**, 045318 (2005).

[24] L.-W. Wang, J. Kim, and A. Zunger, Phys. Rev. B **59**, 5678 (1999).

[25] S. Adachi, *Physical Properties of III-V Semiconductor Compounds* (Wiley, New York, 1992).

[26] G. Bester, A. Zunger, X. Wu, and D. Vanderbilt, Phys. Rev. B **74**, 081305(R) (2006).

[27] M. A. Migliorato, D. Powell, A. G. Cullis, T. Hammerschmidt, and G. P. Srivastava, Phys. Rev. B **74**, 245332 (2006).

[28] A. Schliwa, M. Winkelnkemper, and D. Bimberg, Phys. Rev. B **76**, 205324 (2007).

[29] J. M. Luttinger and W. Kohn, Phys. Rev. **97**, 869 (1955).

[30] T. B. Bahder, Phys. Rev. B **41**, 11992 (1990).

[31] S. Tomić, A. G. Sunderland, and I. J. Bush, J. Mater. Chem. **16**, 1963 (2006).

[32] M. G. Burt, J. Phys.: Condens. Matter **4**, 6651 (1992).

[33] B. A. Foreman, Phys. Rev. B **56**, R12748 (1997).

[34] V. Mlinar and F. M. Peeters, J. Mater. Chem. **17**, 3687 (2007).

[35] H.-B. Wu, S. J. Xu, and J. Wang, Phys. Rev. B **74**, 205329 (2006).

[36] X. Cartoixà, D. Z. Y. Ting, and T. C. McGill, J. Appl. Phys. **93**, 3974 (2003).

[37] P. Lawaetz, Phys. Rev. B **4**, 3460 (1971).

[38] B. Jogai, J. Appl. Phys. **88**, 5050 (2000).

[39] I. Vurgaftman, J. R. Meyer, and L. R. Ram-Mohan, J. Appl. Phys. **89**, 5815 (2001).

[40] Calvin Yi-Ping Chao and S. L. Chuang, Phys. Rev. B **46**, 4110 (1992).

[41] S.-H. Wei and A. Zunger, Phys. Rev. B **60**, 5404 (1999).

[42] G. A. Narvaez, G. Bester, and A. Zunger, J. Appl. Phys. **98**, 043708 (2005).

[43] W. Sheng, S.-J. Cheng, and P. Hawrylak, Phys. Rev. B **71**, 035316 (2005).

[44] W. Sheng and J.-P. Leburton, Phys. Rev. B **64**, 153302 (2001).

[45] A. Franceschetti, H. Fu, L. W. Wang, and A. Zunger, Phys. Rev. B **60**, 1819 (1999).